Journal of *Fungi*

MDPI

Article

Preliminary Structural Elucidation of β-(1,3)-glucan Synthase from *Candida glabrata* Using Cryo-Electron Tomography

Cristina Jiménez-Ortigosa [1,*,†], Jennifer Jiang [2,3,†], Muyuan Chen [4], Xuyuan Kuang [2,3,5], Kelley R. Healey [6], Paul Castellano [2,3], Nikpreet Boparai [2,3], Steven J. Ludtke [4], David S. Perlin [1] and Wei Dai [2,3,*]

1 Hackensack Meridian Health-Center for Discovery and Innovation, 111 Ideation Way, Nutley, NJ 07110, USA; david.perlin@hmh-cdi.org
2 Department of Cell Biology and Neuroscience, Rutgers, The State University of New Jersey, 604 Allison Road, Piscataway, NJ 08854, USA; jj549@rutgers.edu (J.J.); kxy700@126.com (X.K.); paulcastellano621@gmail.com (P.C.); nkb60@scarletmail.rutgers.edu (N.B.)
3 Institute for Quantitative Biomedicine, Rutgers, The State University of New Jersey, 174 Frelinghuysen Road, Piscataway, NJ 08854, USA
4 Department of Biochemistry and Molecular Biology, Baylor College of Medicine, 1 Baylor Plaza, Houston, TX 77030, USA; Muyuan.Chen@bmc.edu (M.C.); sludtke@bcm.edu (S.J.L.)
5 Department of Hyperbaric Oxygen, Central South University, Changsha 410008, China
6 Department of Biology, William Paterson University, 300 Pompton Road, Wayne, NJ 07470, USA; healeyk3@wpunj.edu
* Correspondence: cristina.jimenez-ortigosa@hmh-cdi.org (C.J.-O.); wd157@dls.rutgers.edu (W.D.)
† These authors have contributed equally to this work.

Abstract: Echinocandin drugs have become a front-line therapy against *Candida* spp. infections due to the increased incidence of infections by species with elevated azole resistance, such as *Candida glabrata*. Echinocandins target the fungal-specific enzyme ß-(1,3)-glucan synthase (GS), which is located in the plasma membrane and catalyzes the biosynthesis of ß-(1,3)-glucan, the major component of the fungal cell wall. However, resistance to echinocandin drugs, which results from hotspot mutations in the catalytic subunits of GS, is an emerging problem. Little structural information on GS is currently available because, thus far, the GS enzyme complex has resisted homogenous purification, limiting our understanding of GS as a major biosynthetic apparatus for cell wall assembly and an important therapeutic drug target. Here, by applying cryo-electron tomography (cryo-ET) and subtomogram analysis, we provide a preliminary structure of the putative *C. glabrata* GS complex as clusters of hexamers, each subunit with two notable cytosolic domains, the N-terminal and central catalytic domains. This study lays the foundation for structural and functional studies of this elusive protein complex, which will provide insight into fungal cell wall synthesis and the development of more efficacious antifungal therapeutics.

Keywords: *Candida glabrata*; glucan synthase (GS); cryo-electron tomography (cryoET)

Citation: Jiménez-Ortigosa, C.; Jiang, J.; Chen, M.; Kuang, X.; Healey, K.R.; Castellano, P.; Boparai, N.; Ludtke, S.J.; Perlin, D.S.; Dai, W. Preliminary Structural Elucidation of β-(1,3)-glucan Synthase from *Candida glabrata* Using Cryo-Electron Tomography. *J. Fungi* **2021**, *7*, 120. https://doi.org/10.3390/jof7020120

Academic Editor: Brian Monk
Received: 4 December 2020
Accepted: 2 February 2021
Published: 6 February 2021

1. Introduction

Invasive mycoses have become a significant threat to public health, affecting over a billion people globally and causing over 1.1 million deaths per year. Species from the genera *Aspergillus*, *Candida* and *Cryptococcus* are the most common human pathogenic fungi accounting for a wide variety of invasive and superficial fungal infections. Underlying health conditions such as asthma, acquired immunodeficiency syndrome (AIDS), diabetes, cancer, organ transplantation, and use of corticosteroid therapy are important risk factors for invasive disease. Timely and appropriate antifungal treatment is crucial for the successful outcome of invasive fungal infections [1–4].

The fungal cell wall is an essential dynamic structure that undergoes extensive remodeling necessary for growth, survival, fungal morphogenesis and pathogenesis, and protection against osmotic and mechanical stresses. Since the fungal cell wall does not have

a mammalian counterpart, it is an excellent target for new antifungal therapies [5]. Fungal cell walls are formed by a complex matrix of polysaccharides and proteins covalently cross-linked to one another, and are organized into layers: a more structured, homogeneous inner layer composed of chitin and β-(1,3)-glucan, and a more heterogeneous outer layer whose composition varies with the growth stage and the fungal species [6] (Figure 1). β-(1,3)-glucan, the most abundant structural component of the fungal cell wall, is synthesized by an enzyme complex whose catalytic subunit is embedded in the plasma membrane and presumably acts as a pore for extrusion of newly synthesized linear β-(1,3)-glucan chains into the cell wall where they assemble and are further modified [7].

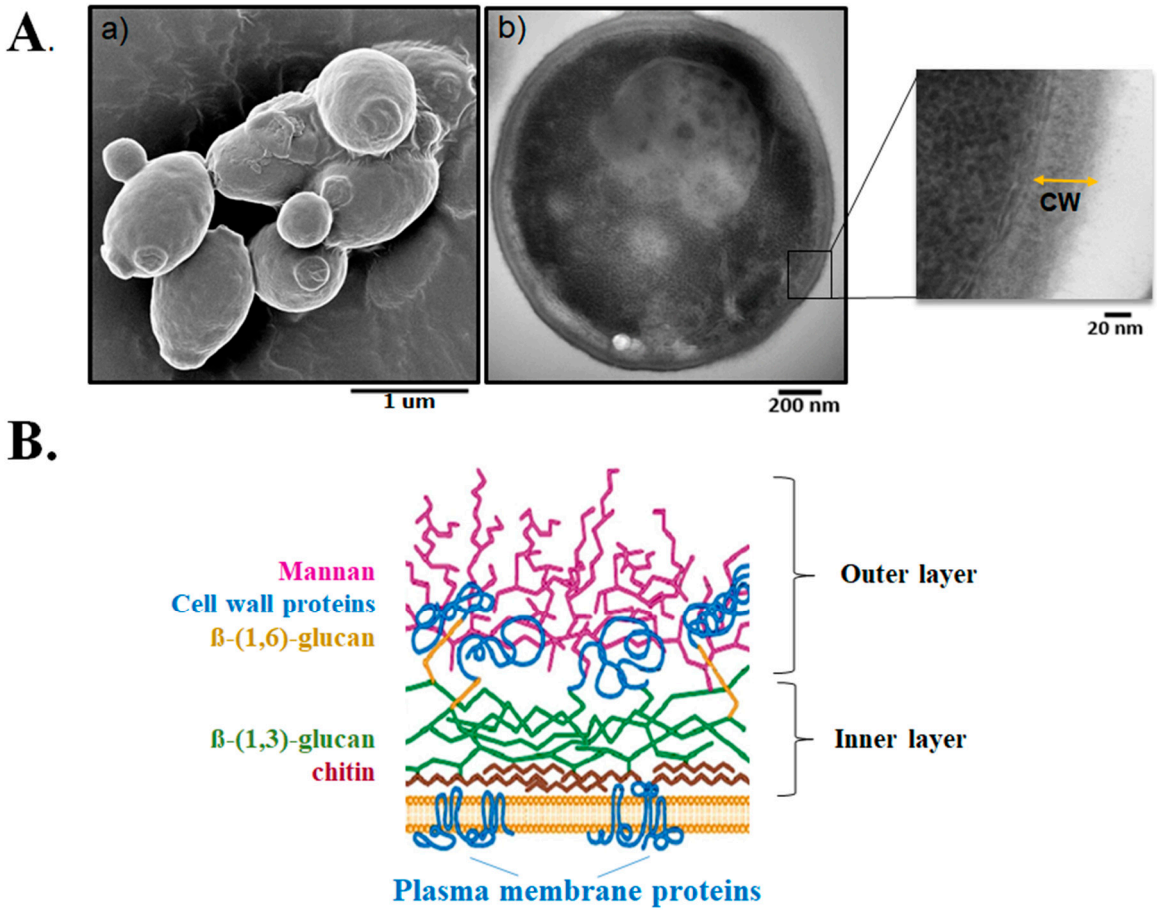

Figure 1. (**A**) *Candida glabrata* cells under (**a**) scanning electron microscope and (**b**) transmission electron microscope (CW = cell wall). (**B**) Schematic representation of the composition and organization of the major components of the fungal cell wall in *Candida* spp. (Figure adapted from [6]).

Candida glabrata has emerged as a common cause of life-threatening fungal infections in many clinical settings in the United States due to its ability to acquire resistance to widely used azole antifungals [8]. As such, the echinocandin antifungals (caspofungin, anidulafungin, and micafungin) are now the preferred front-line therapy against *C. glabrata* and other *Candida* species [9]. They alter the cell wall integrity via inhibition of the catalytic subunit of the enzymatic complex β-(1,3)-glucan synthase (GS), which is responsible for β-(1,3)-glucan biosynthesis [10]. Echinocandin resistance remains a rare event but appears to be on the rise in response to increasing clinical use [11,12]. Reduced susceptibility to echinocandins has been associated with amino acid substitutions in highly conserved hot-spot regions of the *FKS1* and *FKS2* genes, which encode the catalytic subunits of the GS [13]. Despite its critical role in cell wall biosynthesis and as an acclaimed and highly successful drug target, the GS enzyme complex has eluded homogenous purification, limiting our knowledge about its overall three-dimensional organization and the structural mechanisms

underlying β-(1,3)-glucan synthesis [14]. Therefore, direct structural information is needed to better understand GS as an important biosynthetic machine.

Despite the universal role of membrane proteins in various cellular functions, sample purification of these proteins remains a key bottleneck to unraveling their architecture. Conventional structural techniques either require extraction of the protein of interest from its native environment or membrane protein reconstitution in nanodiscs and liposomes [15–17]. Cryo-electron tomography (cryoET) has become the preferred method to characterize the structure of membrane proteins, particularly those that are difficult to purify or crystallize [18,19]. One advantage of cryoET is the ability to directly visualize the cellular landscape and determine the structural dynamics and spatial organization of biomolecules and macromolecular machines from various organisms within their native environment [20–22]. Advances in cryoET technology and subtomogram averaging have enabled structural exploration and detailed characterization of cellular processes in yeast cells [23–25]. Here, we apply cryoET and subtomogram analysis to determine the structure and spatial distribution of the putative GS complex in *C. glabrata*.

2. Materials and Methods

2.1. Strains

Candida glabrata 2001/CBS138 and 200989 (CBS138 his-/trp-/ura-) strains were obtained from the American Type Culture Collection (ATCC, Manassas, VA, USA) and the *FKS1* gene knockout (200989Δ*fks1*::*ScURA3*) was a gift from S. Katiyar (Drexel University College of Medicine) [26]. A gap-repair approach, as described in [27], was used to constitutively express *C. glabrata FKS1*. Plasmid pCN-PDC1 (contains nourseothricin resistance marker, a strong promoter (*PDC1*) and *C. glabrata CEN/ARS*) [28] was linearized with EcoRV and treated with alkaline phosphatase (New England Biolabs, Ipswich, MA, USA). The coding region of *FKS1* was amplified with primers that contain overhang regions homologous to each side of the EcoRV restriction site (Table 1). Competent yeast cells were then co-transformed with the purified PCR product and EcoRV-linearized pCN-PDC1. Following the transformation, cells were subjected to a 3-h outgrowth in YPD broth followed by selection on YPD agar medium supplemented with 100 μg/mL nourseothricin (Jena Bioscience, Jena, Germany). All transformants were PCR screened for construct presence and the entire *FKS1* gene insert was subsequently sequenced to confirm wild type sequence (see Table 1 for primers). The Δ*fks1* transformants were also screened for susceptibility to FK506, an *FKS2* inhibitor, (Invivogen, San Diego, CA, USA) to ensure proper *FKS1* expression from plasmid (p*FKS1*). Cells that express *FKS1* exhibit FK506 resistance while the Δ*fks1* parental cells are susceptible [26]. For controls, wild type and Δ*fks1* cells were also transformed with the empty vector.

2.2. RNA Extraction and Quantitative RT-PCR

Cells were grown in YPD or YPD supplemented with 100 μg/mL nourseothricin (plasmid-carrying strains) to mid-logarithmic phase. Total RNA was extracted using the RNeasy Mini kit (Qiagen Science, Germantown, MD, USA) according to the manufacturer's instructions and stored at −80 °C. The concentration and purity of the RNA was determined using a UV spectrophotometer (NanoDrop One; Thermo Fisher Scientific, Waltham, MA, USA) by measuring the absorbance at 230 (OD230), 260 (OD260) and 280 nm (OD280). The integrity of the RNA was further checked by electrophoresis through 1% denaturing and nondenaturing agarose gels. *FKS1* and *FKS2* expression levels were measured by RT-PCR.

Table 1. Oligonucleotides used in this study.

Primer †	Application	Sequence (5′–3′) ‡
pCN-PDC1-FKS1F	Gap-repair	CAATTGCCAAAAAACATTAACATCTAGAACTAGTGGATCCCCCGGGCTG-CAGGAATTCATGTCTTACAATAATAACGGAC
pCN-PDC1-FKS1R	Gap-repair	AATATTGTTGATGGTGGTAGCTGTGGGTTGTGTTCTCGAGGTCGACGG-TATCGATAAGCTTTTATTTGATTGTAGACCAGG
pCN-PDC1F	PCR/sequence	GAGACCAGACTAATACAACTG
pCN-reverse	PCR/sequence	GTTGCCTGCTACGTAAAGTG
CgFKS1c128R	Sequence	GCCATAGCGATGGCATTAGG
CgFKS1c207F	Sequence	CAAGAAATGGTACTTCGCCG
CgFKS1c594F	Sequence	CCTCCTTTGCACCTTTGCAT
CgFKS1c828F	Sequence	TTTACCGTTTTGACTCCTCAC
CgFKS1c999F	Sequence	CCACATGAACTGGAAAACGC
CgFKS1c1214F	Sequence	GAATGCCCTATTACGTGGTG
CgFKS1c1446F	Sequence	GTTGCTTTTCGGTACCGTTG
CgFKS1c1649F	Sequence	GGGTTCTTGAAGGTTTCAACT
CgFKS1expF	qRT-PCR	CAATTGGCAGAACACCGATCCCAA
CgFKS1expR	qRT-PCR	AGTTGGGTTGTCCGTACTCATCGT
CgFKS2expF	qRT-PCR	TACCAACCAGAAGACCAACAGAATGG
CgFKS2expR	qRT-PCR	TCACCACCGCTGATGTTTGGGT
CgRDN5.8F	qRT-PCR	CTTGGTTCTCGCATCGATGA
CgRDN5.8R	qRT-PCR	GGCGCAATGTGCGTTCA

† Numbers in primer names correspond to amino acid location within the coding region (c). ‡ Underlined regions of gap-repair cloning primers correspond to *C. glabrata FKS1* sequences, and nonunderlined regions correspond to sequences on pCN-PDC1 surrounding EcoRV restriction site.

All qPCR reactions were performed in a 25-µL reaction mixture consisting of 12.5 µL of 2X One Step RT-PCR buffer (One Step SYBR Ex Taq qRT-PCR kit; TaKaRa Bio Inc., Mountain View, CA, USA), 0.2 µM of each primer, 0.5 µL Takara Ex Taq HS (5 U/µL), 0.5 µL RT Enzyme Mix, and 2 µL of RNA (5 ng/µL) on an Mx3005P real-time instrument (Stratagene, La Jolla, CA, USA). Optimal thermal cycling conditions consisted of 42 °C for 5 min for the reverse transcription, followed by an initial denaturation step at 95 °C for 10 s, 40 cycles of 95 °C for 5 s (denaturation), 60 °C for 20 s (annealing and extension). The experiments were carried out in triplicate for each data point. The relative quantification in gene expression was determined using the $2^{-\Delta\Delta Ct}$ method [29] with expression level of the gene *RDN5.8* for normalization [30]. The primers used are listed in Table 1.

2.3. Western Blotting

Fks1 expression levels were determined in total cellular extracts by Western blot analysis as described previously [31] from the following strains CBS138, 200989 Δ*fks1*, 200989 + pCN-PDC1-*FKS1* and 200989 Δ*fks1* + pCN-PDC1-*FKS1*. Blotted proteins were incubated with anti-Fks1 primary antibody (GenScript Biotech, Piscataway, NJ, USA) at a dilution of 1:5000 in 2% TBST at 4 °C for 16 h. Washed membranes were incubated with horseradish peroxidase-conjugated secondary antibody (anti-rabbit; Cell Signaling Technology, Boston, MA, USA) at 1:3000 dilution for 1 h. Bands were visualized with Novex ECL Chemiluminescent substrates (Thermo Fisher Scientific, Waltham, MA, USA) following the manufacturer's instructions.

2.4. Isolation of Enriched Plasma Membrane Fractions

Enriched plasma membrane fractions were isolated from CBS138 (wild type, WT) and 200989 Δ*fks1* + pCN-PDC1-*FKS1* (KH238) strains. Cells were grown in YPD (yeast extract 1%, peptone 2%, dextrose 2%) or YPD supplemented with 100 µg/mL nourseothricin for the plasmid-carrying strain, to mid-logarithmic phase. The cells were collected by centrifugation, washed twice with water and incubated 1 h at 30 °C with 1% ß-mercaptoethanol (MilliporeSigma, Burlington, MA, USA). After incubation, cells were washed twice with water and resuspended in buffer S (1M sorbitol, 10 mM HEPES, pH 6.5). To remove the cell

wall and generate protoplasts, lytic enzymes from *Trichoderma harzianum* (MilliporeSigma, Burlington, MA, USA) were added to buffer S, following an incubation overnight at room temperature with gentle shaking. The generation of protoplasts was monitored under the microscope, to assure that at least 90% of the cells lacked the cell wall. The protoplasts were collected by centrifugation and washed twice with PBS1X supplemented with a phosphatase and protease inhibitor cocktail (MilliporeSigma, Burlington, MA, USA) to lyse them and then, loaded into a one-step sucrose gradient. Purified plasma membranes were recovered at the 53.5–43.5% (wt/wt) sucrose interface of a step gradient containing 1 mM EDTA, 1 mM DTT, and 10 mM Tris (pH 7.0) after centrifugation for 3 h at 39,000 rpm in a SW41 rotor (Beckman Coulter, Brea, CA, USA). The membranes were washed for 1 h at 39,000 rpm in a 50.2 Ti rotor (Beckman Coulter, Brea, CA, USA) and resuspended in PBS1X with a phosphatase and protease inhibitors, kept at 4 °C and then plunge frozen before visualization under the cryo-electron microscope.

2.5. Preparation of EM Grids

The enriched plasma membrane fractions obtained from wild type and KH238 strains were mixed with 6 nm gold particles as fiducial markers to facilitate tilt series alignment during image processing. An aliquot of 3.5 µL of extracted plasma membrane samples was applied to glow discharged Quantifoil holey grids (R2.0/1.0, Cu, 200 mesh; Quantifoil) prior to vitrification using a Leica EM GP plunger (Leica Microsystems, Buffalo Grove, IL, USA) in a humidity (95%) and temperature (20 °C) controlled chamber. Plunge-frozen grids were stored in a liquid nitrogen dewar flask until imaging.

2.6. Tomography Data Collection

Images and tilt series of the samples were collected on a Talos Arctica cryo-electron microscope (Thermo Fisher Scientific, Waltham, MA, USA) operated at 200 kV, equipped with a post-column BioQuantum energy filter (the slit was set to 20 eV) and a K2 direct electron detector. Automated data collection was performed using SerialEM [32] under the following conditions: 49,000× microscope magnification, spot size 8, 100-µm condenser aperture, and defocus range of −5–−3 µm. The image pixel size was 2.73 Å/pixel. Tilt series ranged from −69° to 69° at 3° step increments. A total of 625 and 272 tilt series of plasma membranes from wild type and KH238 strains were collected, respectively, in counting mode with a cumulative dose of 60–80 $e^-/Å^2$. At each tilt angle, 10 dose fractionation frames were collected to correct for stage drift and beam-induced motion during exposure. A subset of tilt series of wild type yeast plasma membranes were collected from the Thermo Fisher Titan Krios microscope at Purdue University at 42,000× microscope magnification, and defocus at −0.5 µm with Volta phase plate. The image pixel size was 2.80 Å/pixel. This subset was used for generation of an initial model for symmetry analysis and preliminary structural analysis.

2.7. Tomography Data Processing

Movie frames for each tilt series were aligned using UCSF MotionCor2 [33]. Alignment of motioned-corrected tilt series and reconstruction of tomograms were performed using the latest EMAN2 tomography workflow [34]. For wild type plasma membranes, tomograms with strong image contrast and detectable ring-like structures were selected for subsequent subtomogram averaging and analysis. From these selected tomograms, a *de novo* initial model was generated with ~50 extracted particles using a box size of 128^3 pixels. To achieve isotropic resolution for the *de novo* initial model, a subset of subvolumes with side views of the putative GS structures in context of membrane features was included to compensate for the preferred orientation of the particles due to membrane geometry on grids. Five iterations of the EMAN2 reference-free initial model generation routine were performed with no symmetry specified. After alignment to the symmetry axis, the initial model was used for subsequent subtomogram refinement using a larger dataset of 1818 particles. Rotational cross-correlation analysis was performed on the initial

average map to assess structural symmetry. 2D plots of coefficients showed signature peaks indicative of C6 symmetry. A second round of refinement was performed with C6 symmetry specified during subtomogram refinement and averaging.

Plasma membranes isolated from Fks1-overexpressing cells featured greater abundance of the larger ring-like structures. A larger set of 5108 particles was extracted for subtomogram averaging. Following a similar subtomogram averaging and analysis procedure as detailed above, with a box size of 168^3 pixels, a final map with a global resolution of 14 Å was achieved as determined by the Fourier shell correlation (FSC) of density maps from two independent halves of the entire dataset [35].

Visualization, segmentation and domain analysis of 3D maps and subunits were done using Chimera (University of California, San Francisco) [36].

2.8. Analysis of GS Spatial Distribution

Tomograms containing >250 putative GS particles were used to evaluate the spatial distribution of the putative GS complexes within the clusters. Coordinates of the center of the complexes were used for subsequent nearest neighbor analysis. Within a cluster of putative GS complexes, the nearest neighbor of a particle was defined as the particle within the shortest linear distance. The nearest neighbor distance was computed as the distance from the center of a particle to the center of its nearest neighbor. For 2D average analysis, 183 subtomograms containing patches of putative GS complexes were extracted using a box size of 256^3 pixels and then subjected to a 30 Å low pass filter to remove high frequency noises. A 2D average was generated by reference-free 2D refinement using the projections of the 3D subtomograms of these protein complex clusters. Unit cell annotations were done using the measurement functionality available in EMAN2.

3. Results

3.1. Identification of Two Populations of Ring-Like Structures in C. glabrata Plasma Membranes

To examine the protein structures present in *C. glabrata* plasma membrane, we first generated protoplasts, which are cell wall-less yeast cells that are viable when incubated in an osmotically stabilizing liquid nutrient medium and can synthesize a new cell wall and revert to a normal phenotype. From the protoplasts of *C. glabrata* wild type strain CBS138, we collected the enriched plasma membrane fraction from a sucrose gradient and imaged these membrane fragments using the Talos Arctica cryo-electron microscope. We examined over 600 tomograms and found that 8–10% contained clusters of a ring-like structure with an approximate diameter of 170 Å. These clusters were heterogeneously distributed on the plasma membranes, and primarily found in patches across large membrane regions (Figure 2A,C; blue arrows, and Supplementary Movie S1). In addition, a smaller ring-like structure, with a diameter of 125 Å, was observed in less frequent and more loosely packed clusters (Figure 2B,D; pink arrows, and Supplementary Movie S2). The smaller rings were markedly less abundant compared to the larger ring-like structures and were detected in less than 1% of all tomograms.

To determine whether the large or small ring-like structures corresponded to the uncharacterized β-(1,3)-glucan synthase (GS), we constructed strains that constitutively express the *FKS1* gene. We first measured *FKS* gene expression to confirm that the strains carrying the plasmid pCN-PDC1-*FKS1* were indeed overexpressing the *FKS1* gene. RNA was isolated from cells harvested in mid-log growth phase and levels of *FKS1* and *FKS2* mRNA were compared to that of the wild type strains CBS138 and 200989. We observed a 3- and 4-fold increase in the expression level of *FKS1* in the plasmid-containing strains 200989 + p*FKS1* and 200989 Δ*fks1* + p*FKS1*, respectively, when compared to the expression levels of both wild type strains. *FKS2* expression levels also increased by 2-fold in the plasmid-containing strains, similar to the levels observed in the knock-out strain (Table 2). Western blot analysis showed that the strains carrying the plasmid contained a higher abundance of the Fks1 protein compared to the wild type strain (Figure 3A). For further analysis, we used the strain 200989 Δ*fks1* + pCN-PDC-*FKS1* (KH238).

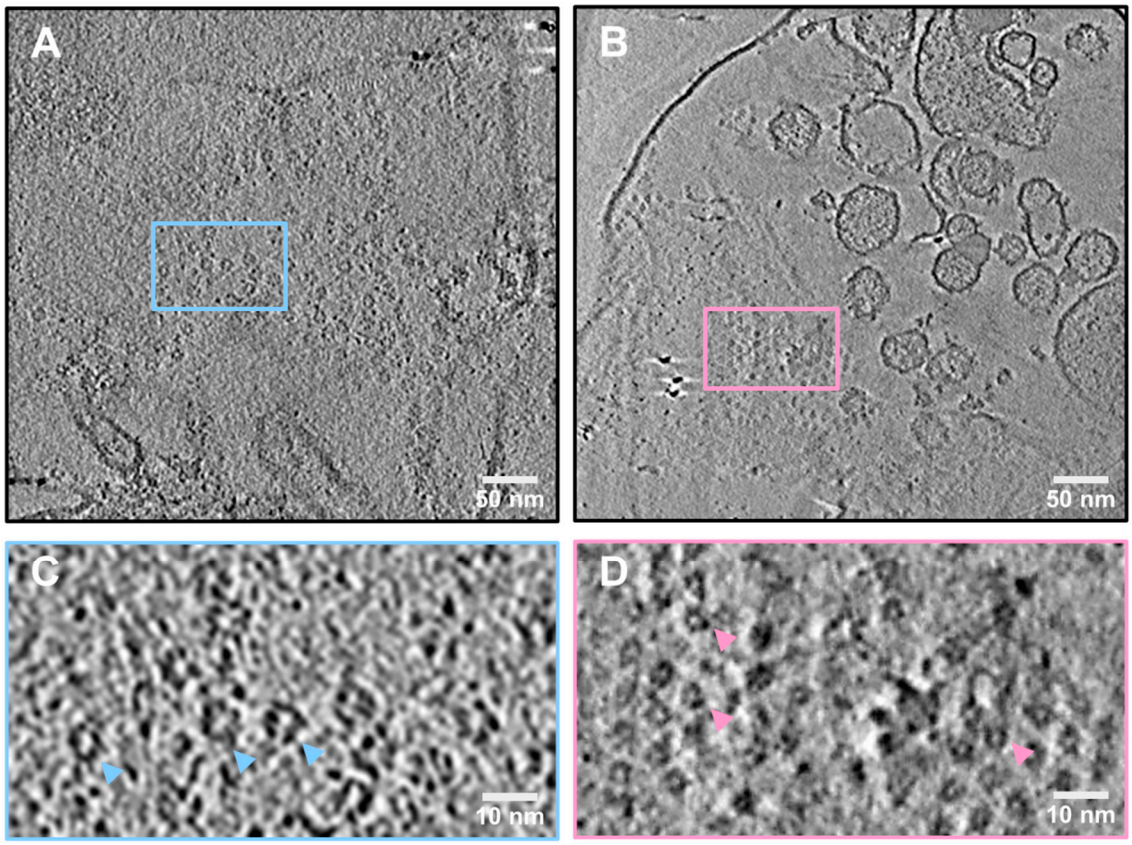

Figure 2. Cryo-electron tomography (cryoET) revealed two ring-like structures in plasma membranes of *Candida glabrata* CBS138 strain. (**A**) Slice view of plasma membranes with clusters of loosely packed, 170 Å diameter large ring-like structures. (**B**) Slice view of a representative tomogram showing the small 125 Å ring-like structures. Electron-dense particles are gold fiducials. (**C**) Zoomed-in slice view of the large ring-like structures (blue arrows) boxed in (**A**). (**D**) Zoomed-in slice view of the small ring-like structures (pink arrows) boxed in (**B**).

Table 2. Expression profiling of the *FKS* genes compared to the wild-type strains CBS138 and 200989.

Strain	*FKS1* Fold-Change	*FKS2* Fold-Change
200989 Δ*fks1*	0	2.16 ± 0.22
200989 + pCN-PDC1-FKS1	2.72 ± 0.14	1.85 ± 0.46
200989 Δ*fks1* + pCN-PDC1-*FKS1* (KH238)	4.22 ± 0.72	2.40 ± 0.82

To examine whether the overexpression of Fks1 shifts the abundance and distribution of the large or small ring-like structures, we evaluated tomograms collected from the strain overexpressing Fks1 (KH238) and compared the data to those from the wild type sample. Notably, the relative abundance of the large ring structure increased significantly in the KH238 strain compared to the wild type (Figure 3B, blue arrows; Figure 3C, orange arrows, and Movie S3). About 22% of tomograms collected from Fks1-overexpressing plasma membranes contained clusters of the large rings. Overexpression of Fks1 also shifted the packing of the large ring-like structures within the clusters. Nearest neighbor analysis revealed that in plasma membranes of wild type cells, large ring-like structures within clusters formed a 2D distribution that followed a Gaussian distribution with a defined peak at 240 Å (Figure 3D; blue). Overexpression of Fks1 shifted the organization of these protein clusters to a narrower distribution with a peak at 180 Å (Figure 3D; orange), which is slightly larger than the measured diameter of these large ring-like densities (~170 Å). 2D averaging of patches of these clusters confirmed the semicrystalline array packing of the large ring-like structures, with minimal spacing between neighboring complexes

(Figure 3E). Taken together, biochemical and structural data suggest that these large ring-like structures are putative GS complexes.

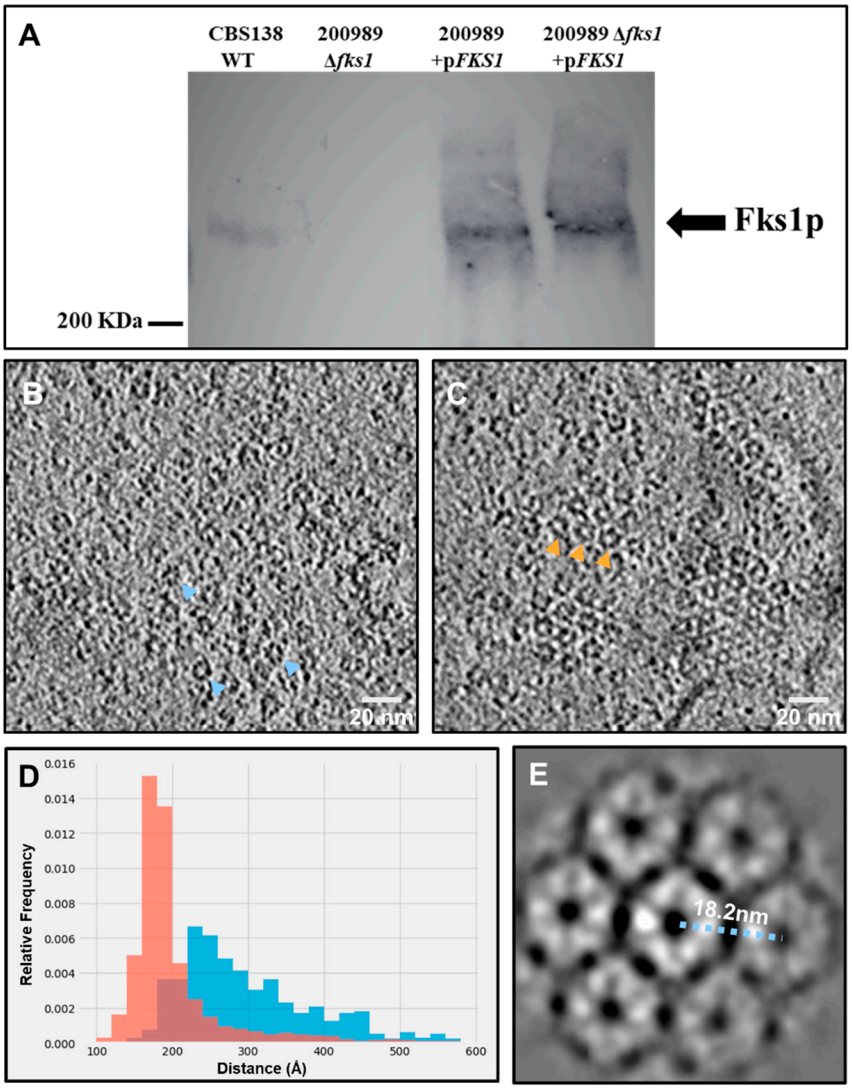

Figure 3. Large ring-like structures in *Candida glabrata* overexpressing Fks1 strain. (**A**) Expression levels of Fks1. *C. glabrata* cells from the different strains were grown on liquid YDP with (plasmid-carrying strains) or without 100 µg/mL nourseothricin until mid-log phase, and proteins were extracted using the TCA method. p*FKS1* = pCN-PDC-*FKS1* and KH238 strain = 200989 Δ*fks1*+ p*FKS1*. (**B**) Slice view of a representative tomogram showing a patch of the large ring-like structures from the wild type strain (blue arrows). (**C**) Slice view clusters of the large ring-like structures in membranes from the strain overexpressing Fks1 (KH238) (orange arrows). (**D**) Histogram showing nearest neighbor distance of the large ring-like particles within clusters from the KH238 (orange) and wild type (blue) strains. (**E**) 2D average of the semicrystalline array composed of the large ring-like structures.

3.2. Structural Determination of Putative Glucan Synthase Complexes by Subtomogram Averaging

To further investigate the domain organization of the putative GS complexes, we performed subtomogram averaging (Figure S1) with particles extracted from plasma membranes of both wild type and KH238 strains. The overall morphology between the two 3D subtomogram averages from wild type and Fks1-overexpressing cells are similar (Figure 4A,B). A higher resolution map of the putative GS complex from membranes of the KH238 strain, resolved at ~14 Å determined by Fourier shell correlation (FSC) (Figure 4C), was obtained due to higher abundance of the protein complexes.

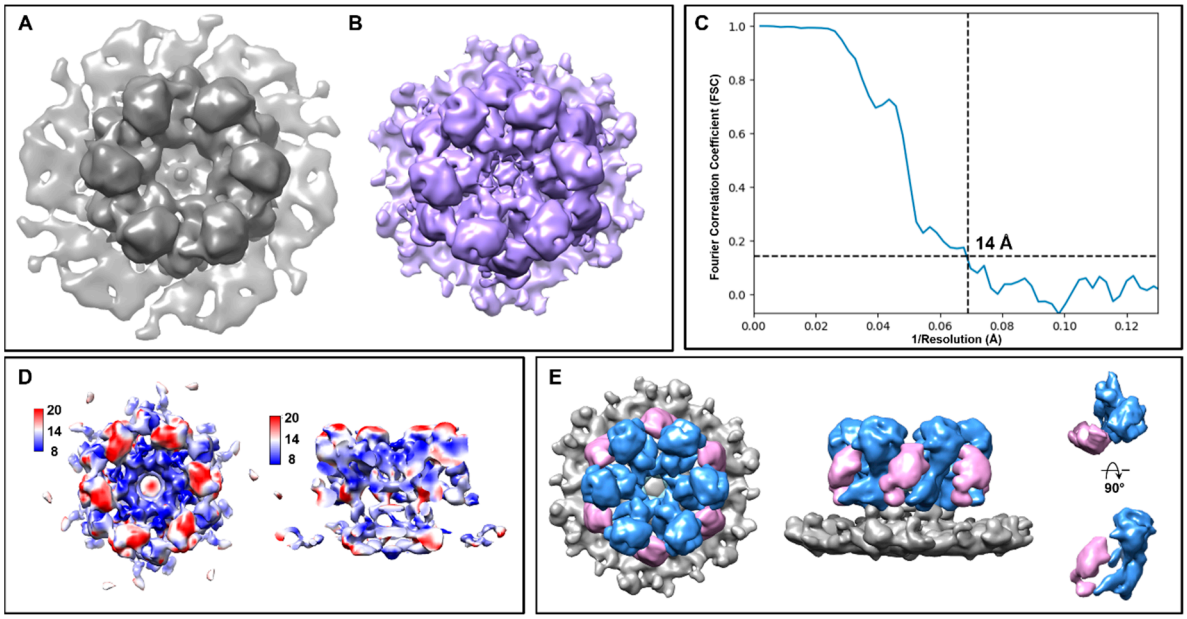

Figure 4. Structural analysis of putative glucan synthase (GS) complexes. (**A**) Isosurface, top views of the putative GS structure from wild type (**A**)—gray and KH238 (**B**)—purple plasma membranes. (**C**) Resolution assessment of the subtomogram average of putative GS complexes from the Fks1 overexpression strain by Fourier shell correlation (FSC). (**D**) Top (left) and cutaway side (right) views of the local resolution evaluation of the subtomogram average from the Fks1-overexpressing strain. (**E**) Top (left) and side (middle) views of the segmented putative GS density map from the Fks1-overexpressing strain. The cytosolic N-terminal and central catalytic domains in a monomeric unit of the complex are annotated pink and blue, respectively.

The putative GS complexes display dominant C6 symmetry with a central pore measuring 62 Å in diameter (Figure 4B, Movie S4;). From local resolution maps, the overall conformation of the complex is relatively stable and rigid with the exception at the top region of the central domain (Figure 4D; red). Each monomeric unit in the hexameric complex clearly showed two extramembrane domains protruding towards one side (Figure 4E). Based on the topological model of the Fks1 protein in *Saccharomyces cerevisiae* [14], these two domains can be assigned as the cytosolic, N-terminal (Figure 4E, Movie S4; pink) and central catalytic domains (Figure 4E, Movie S4; blue), respectively. While the N-terminal domain adopts a globular conformation, the larger central domain is defined by a top globular domain, a neck region, and a basal domain that connects the protein complex to the underlying membrane. Interactions between neighboring monomers of the putative GS complex appear to be mediated by densities extending from the apical region of the N-terminal domain and the central catalytic domain. The central pore of the complex is formed by the basal region of the central catalytic domain. The geometry of plasma membranes on the grids results in preferred orientation, and therefore lower number of side views in our tomograms. Consequently, the transmembrane domain of the putative GS complex is less well-resolved.

4. Discussion

Glucan synthase (GS) is an ideal drug target for antifungal therapy since it is an essential and unique enzyme in fungi. This value has been borne-out by the clinical success of the echinocandin class of drugs. However, despite more than 40 years of intense research, major advances in elucidating the structure of the GS complex have proven unsuccessful and have not advanced beyond basic solubilization and product entrapment [7]. Despite enrichment of enzymatic activity, there has not been a report of significant purification of the fungal GS to advance structure-based studies. Here, we present the first study describing an initial structure of the putative GS complex from the pathogen *Candida*

glabrata using cryoET, a powerful technique for 3D visualization of cellular structures, especially membrane proteins in their native state.

Tomograms collected from the enriched plasma membrane fractions revealed clusters of ring-like structures distributed in patches in both the wild type and the Fks1-overexpressing (KH238) strains after protoplast formation. Protoplasts can synthesize a new cell wall and revert to normal cells, when incubated in an osmotically stabilizing liquid nutrient medium. The regeneration of the cell wall starts with the formation of microfibrils of chitin and ß-(1,3)-glucan that are laid onto the cell surface [37]. Previous studies in our laboratory have shown that cell wall regeneration may occur in well-defined, electron-dense areas localized throughout the plasma membrane (and Figure 5) consistent with the distribution pattern of clusters observed in tomograms.

After the application of subtomogram averaging, the putative GS complexes displayed a dominant C6 symmetry, suggesting that the enzyme complex is a hexameric structure. *C. glabrata* contains two *FKS* genes encoding the catalytic subunit of the GS, which share 88% sequence identity and are functionally redundant [26]. GS complexes may be compositionally heterogeneous with catalytic subunits from either Fks1 or Fks2, since the two proteins may adopt similar structures and an oligomeric state in the plasma membranes. The resolution of our current subtomogram average is not sufficient to resolve atomic details required for recognition of conformational differences between the two protein paralogs.

Our structural model showed that each monomer of GS complex contained two extramembrane domains that can be assigned as the cytosolic N-terminal and the central catalytic domains comprising 437 and 660 amino-acids, respectively, based on previous studies [14]. Moreover, we observed densities extending from the apical region of both domains indicating interactions between neighboring monomers. In *S. cerevisiae*, it has been postulated that the GS consists of multiple functional domains required for cell wall biogenesis since mutations in the N-terminal domain led to defects in the synthesis of ß-(1,3)-glucan, and mutations in the central domain resulted in loss of GS catalytic activity [38,39]. We speculate that both cytosolic domains interact with each other and those of adjacent monomers of the complex to form the nascent chains of ß-(1,3)-glucan.

A recent publication on higher plant cellulose synthase proposes that cellulose protofibers are extruded from a narrow channel, 10–15 Å in diameter, within individual monomers of trimeric cellulose synthase complexes [40]. In our subtomogram average of putative GS hexamers, the central catalytic domain is resolved as a solid density without an apparent opening or exit on either side. At the current resolution, we cannot determine if a channel exists in each monomer or whether it would accommodate glucan protofibers. At the center of these putative GS complexes, the basal regions of the central catalytic domain of the six Fks monomers form a transmembrane pore 62 Å in diameter. Atomic resolution maps of the complexes that clearly delineate the position of the substrate binding pocket and the catalytic amino acids are needed to reveal the extrusion mechanism underlying glucan synthesis.

In summary, our preliminary structural study on *C. glabrata* provides an explorative look into the once elusive GS enzymatic complex, offering opportunities for additional structural and functional analyses to better understand the implications of GS in cell wall synthesis, the interactions of the current antifungal drugs with the enzyme and assist the development of more effective antifungal therapeutic strategies.

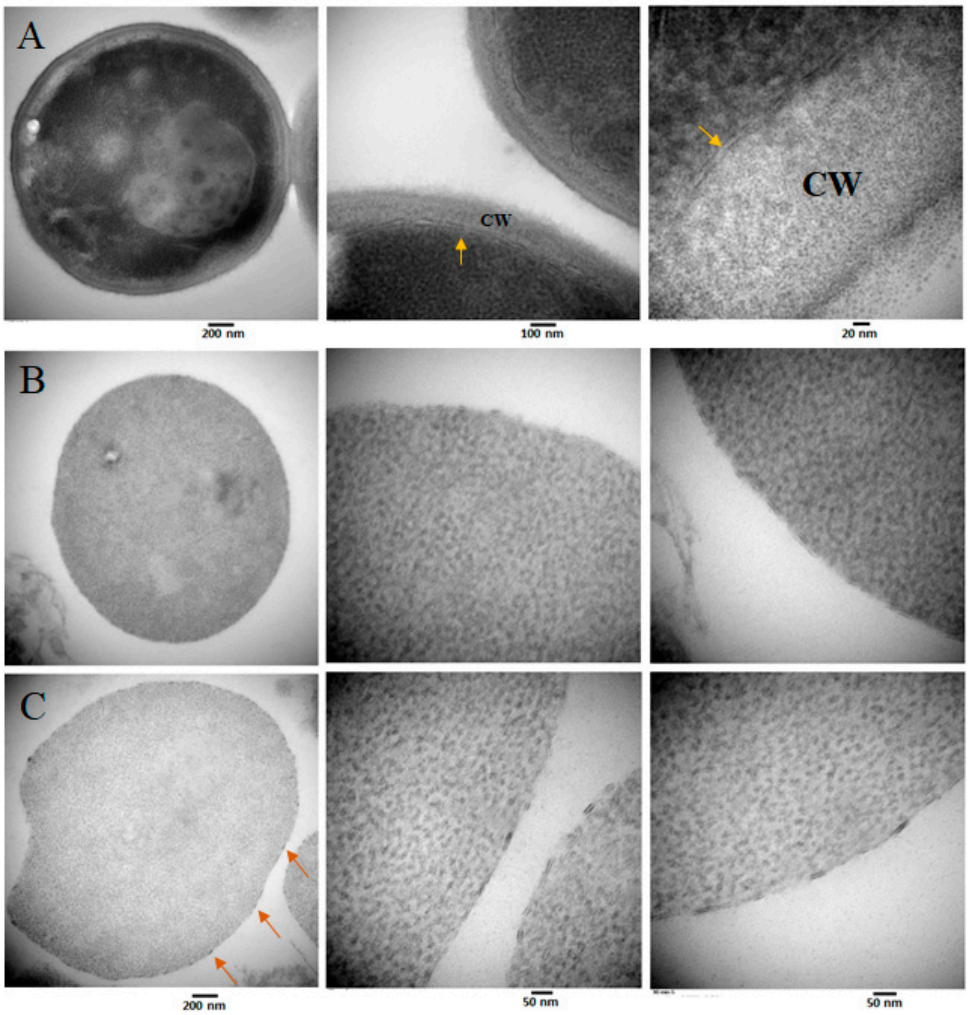

Figure 5. Transmission electron microscopy of (**A**) *Candida glabrata* CBS138 strain growing in log phase. The yellow arrows indicate the plasma membrane. CW = cell wall. (**B**) *C. glabrata* protoplasts after enzymatic removal of the cell wall, and (**C**) regeneration of the *C. glabrata* protoplasts in YPD liquid medium plus sorbitol 1M after 90 min. The orange arrows show electron-dense areas in the plasma membrane, where the synthesis of new components of the cell wall may take place. The size bars for panels B and C are the same.

Supplementary Materials: The following are available online at https://www.mdpi.com/2309-608X/7/2/120/s1. Figure S1. Subtomogram analysis and averaging workflow; Movie S1. Slice views of large ring-like structures from *C. glabrata* CBS138 strain protoplast membrane (https://drive.google.com/file/d/18iT68GkqJXkcelNfGrVo_N6z-_bx2D7a/view?usp=sharing); Movie S2. Slice views of small ring-like structures from *C. glabrata* CBS138 strain protoplast membrane (https://drive.google.com/file/d/18kf0C5KAGJmv4aEa5iM6pK4Bbk3YfOQ3/view?usp=sharing); Movie S3. Slice views of large ring-like structures from *C. glabrata* KH238 strain protoplast membrane (https://drive.google.com/file/d/18lCntJEAlqvCfOPFT-G_ViI_40Guy_5Z/view?usp=sharing); Movie S4. 3D isosurface representation of subtomogram average of the putative GS complex. The map was displayed with different thresholds and rotation. Subunits of the protein complex were segmented and annotated in different colors (https://drive.google.com/file/d/18loLi5Ri5XHrB67jauIS0kN-HwTtuWCw/view?usp=sharing).

Author Contributions: Conceptualization, C.J.-O.; D.S.P. and W.D.; Methodology, C.J.-O.; J.J.; K.R.H.; X.K.; P.C.; M.C. and W.D. Investigation, C.J.-O.; J.J.; M.C.; P.C.; X.K.; N.B.; S.J.L. and W.D. Writing—original draft, C.J.-O.; J.J.; M.C. and W.D.; Writing—review and editing, C.J.-O.; J.J.; D.S.P. and W.D. Supervision, C.J.-O.; D.S.P. and W.D.; Funding acquisition, D.S.P.; S.J.L. and W.D. All authors have read and agreed to the published version of the manuscript.

Funding: This work was supported by the National Institutes of Health (R01AI109025) to D.S.P. and (P011030036319 and R01GM080139) to S.J.L. Tomographic data collected from Purdue University was supported by the National Institutes of Health Midwest Consortium for High Resolution Cryo-electron Microscopy (U24 GM116789-01A1). This research was also partially supported by Rutgers Busch Biomedical Research Grant to W.D.

Institutional Review Board Statement: Not applicable.

Informed Consent Statement: Not applicable.

Data Availability Statement: The data that support the findings of this study are available from the corresponding authors upon reasonable request. Programs used for tomographic data analysis are available from EMAN2.org. Electron density maps of putative GS from wild type and KH238 strains have been deposited in the EMDataBank—accession numbers EMD-23122 and EMD-23123, respectively.

Acknowledgments: We thank Jason Kaelber at Rutgers CryoEM and Nanoimaging Facility and Thomas Klose at Purdue University for their support in data collection.

Conflicts of Interest: Disclosure statement: D.S.P. receives funding from the U.S. National Institutes of Health and contracts with The Centers for Disease Control and Prevention, Amplyx, Astellas, Cidara, and Scynexis. He serves on advisory boards for Amplyx, Astellas, Cidara, Matinas, N8 Medical, and Scynexis. In addition, D.S.P. has an issued U.S. patent concerning echinocandin resistance. The remaining authors declare no potential conflicts of interest.

References

1. Bongomin, F.; Gago, S.; Oladele, R.O.; Denning, D.W. Global and Multi-National Prevalence of Fungal Diseases-Estimate Precision. *J. Fungi.* **2017**, *3*, 57. [CrossRef] [PubMed]
2. Limper, A.H.; Adenis, A.; Le, T.; Harrison, T.S. Fungal infections in HIV/AIDS. *Lancet Infect. Dis.* **2017**, *17*, e334–e343. [CrossRef]
3. GAFFI. Fungal diseases frequency. Global Action Fund for Fungal Infections. 2020. Available online: https://www.gaffi.org/why/fungal-disease-frequency (accessed on 14 October 2020).
4. Belmann, R.; Smuszkiewicz, P. Pharmacokinetics of antifungal drugs: Practical implications for optimized treatment of patients. *Infection* **2017**, *45*, 737–779. [CrossRef]
5. Cortés, J.C.G.; Curto, M.A.; Carvalho, V.S.D.; Pérez, P.; Ribas, J.C. The fungal cell wall as a target for the development of new antifungal therapies. *Biotechnol. Adv.* **2019**, *37*, 107352. [CrossRef] [PubMed]
6. Gow, N.A.R.; Latge, J.-P.; Munro, C.A. The fungal cell wall: Structure, biosynthesis, and function. *Microbiol. Spectrum.* **2017**, *5*. [CrossRef]
7. Douglas, C.M. Fungal beta(1,3)-D-glucan synthesis. *Med. Mycol.* **2001**, *39*, 55–66. [CrossRef] [PubMed]
8. Pappas, P.; Lionakis, M.; Arendrup, M.; Ostrosky-Zeichner, L.; Kullberg, B.J. Invasive candidiasis. *Nat. Rev. Dis. Primers* **2018**, *4*, 18026. [CrossRef]
9. Pappas, P.G.; Kauffman, C.A.; Andes, D.R.; Clancy, C.J.; Marr, K.A.; Ostrosky-Zeichner, L.; Reboli, A.C.; Schuster, M.G.; Vazquez, J.A.; Walsh, T.J.; et al. Clinical Practice Guideline for the Management of Candidiasis: 2016 Update by the Infectious Diseases Society of America. *Clin. Infect. Dis.* **2016**, *62*, e1–e50. [CrossRef]
10. Wiederhold, N.P. The antifungal arsenal: Alternative drugs and future targets. *Int. J. Antimicrob. Agents* **2018**, *51*, 333–339. [CrossRef]
11. Pfaller, M.A.; Castanheira, M.; Lockhart, S.R.; Ahlquist, A.M.; Messer, S.A.; Jones, R.N. Frequency of decreased susceptibility and resistance to echinocandins among fluconazole-resistant bloodstream isolates of *Candida glabrata*. *J. Clin. Microbiol.* **2012**, *50*, 1199–1203. [CrossRef]
12. Alexander, B.D.; Johnson, M.D.; Pfeiffer, C.D.; Jiménez-Ortigosa, C.; Catania, J.; Booker, R.; Castanheira, M.; Messer, S.A.; Perlin, D.S.; Pfaller, M.A. Increasing echinocandin resistance in *Candida glabrata*: Clinical failure correlates with presence of *FKS* mutations and elevated minimum inhibitory concentrations. *Clin. Infect. Dis.* **2013**, *56*, 1724–1732. [CrossRef]
13. Perlin, D.S. Echinocandin Resistance in *Candida*. *Clin. Infect. Dis.* **2015**, *61*, S612–S617. [CrossRef]
14. Johnson, M.E.; Edlind, T.D. Topological and mutational analysis of *Saccharomyces cerevisiae* Fks1. *Eukaryot. Cell* **2012**, *11*, 952–960. [CrossRef]
15. Seto-Young, D.; Perlin, D.S. Effect of membrane voltage on the plasma membrane H(+)-ATPase of *Saccharomyces cerevisiae*. *J. Biol. Chem.* **1991**, *266*, 1383–1389. [CrossRef]
16. Shen, H.; Lithgow, T.; Martin, L. Reconstitution of Membrane Proteins into Model Membranes: Seeking Better Ways to Retain Protein Activities. *Int. J. Mol. Sci.* **2013**, *14*, 1589–1607. [CrossRef] [PubMed]
17. Goers, R.; Thoma, J.; Ritzmann, N.; Di Silvestro, A.; Alter, C.; Gunkel-Grabole, G.; Fotiadis, D.; Muller, D.J.; Meier, W. Optimized reconstitution of membrane proteins into synthetic membranes. *Commun. Chem.* **2018**, *1*, 35. [CrossRef]
18. Lučić, V.; Rigort, A.; Baumeister, W. Cryo-electron tomography: The challenge of doing structural biology in situ. *J. Cell Biol.* **2013**, *202*, 407–419. [CrossRef] [PubMed]

19. Dunstone, M.A.; de Marco, A. Cryo-electron tomography: An ideal method to study membrane-associated proteins. *Philos. Trans. R. Soc. Lond. B Biol. Sci.* **2017**, *372*, 20160210. [CrossRef] [PubMed]
20. Zhu, P.; Liu, J.; Bess, J., Jr.; Chertova, E.; Lifson, J.D.; Grisé, H.; Ofek, G.A.; Taylor, K.A.; Roux, K.H. Distribution and three-dimensional structure of AIDS virus envelope spikes. *Nature* **2006**, *441*, 847–852. [CrossRef]
21. Hampton, C.M.; Strauss, J.D.; Ke, Z.; Dillard, R.S.; Hammonds, J.E.; Alonas, E.; Desai, T.M.; Marin, M.; Storms, R.E.; Leon, F.; et al. Correlated fluorescence microscopy and cryo-electron tomography of virus-infected or transfected mammalian cells. *Nat. Protoc.* **2017**, *12*, 150–167. [CrossRef]
22. Levitan, O.; Chen, M.; Kuang, X.; Cheong, K.Y.; Jiang, J.; Banal, M.; Nambiar, N.; Gorbunov, M.Y.; Ludtke, S.J.; Falkowski, P.G.; et al. Structural and functional analyses of photosystem II in the marine diatom *Phaeodactylum tricornutum*. *Proc. Natl. Acad. Sci. USA* **2019**, *116*, 17316–17322. [CrossRef] [PubMed]
23. Cai, S.; Chen, C.; Tan, Z.Y.; Huang, Y.; Shi, J.; Gan, L. Cryo-ET reveals the macromolecular reorganization of *S. pombe* mitotic chromosomes in vivo. *Proc. Natl. Acad. Sci. USA* **2018**, *115*, 10977–10982. [CrossRef]
24. Gan, L.; Ng, C.T.; Chen, C.; Cai, S. A collection of yeast cellular electron cryotomography data. *GigaScience* **2019**, *8*, giz077. [CrossRef] [PubMed]
25. Ng, C.T.; Gan, L. Investigating eukaryotic cells with cryo-ET. *Mol. Biol. Cell.* **2020**, *31*, 87–100. [CrossRef] [PubMed]
26. Katiyar, S.K.; Alastruey-Izquierdo, A.; Healey, K.R.; Johnson, M.E.; Perlin, D.S.; Edlind, T.D. Fks1 and Fks2 are functionally redundant but differentially regulated in *Candida glabrata*: Implications for echinocandin resistance. *Antimicrob. Agents Chemother.* **2012**, *56*, 6304–6309. [CrossRef]
27. Healey, K.R.; Paderu, P.; Hou, X.; Jimenez-Ortigosa, C.; Bagley, N.; Patel, B.; Zhao, Y.; Perlin, D.S. Differential Regulation of Echinocandin Targets Fks1 and Fks2 in *Candida glabrata* by the Post-Transcriptional Regulator Ssd1. *J. Fungi* **2020**, *6*, 143. [CrossRef] [PubMed]
28. Zordan, R.E.; Ren, Y.; Pan, S.J.; Rotondo, G.; De Las Penas, A.; Iluore, J.; Cormack, B.P. Expression plasmids for use in *Candida glabrata*. *G3 (Bethesda)* **2013**, *3*, 1675–1686. [CrossRef]
29. Livak, K.J.; Schmittgen, T.D. Analysis of relative gene expression data using real-time quantitative PCR and the 2(-Delta Delta C(T)) Method. *Methods* **2001**, *25*, 402–408. [CrossRef]
30. Li, Q.; Skinner, J.; Bennett, J.E. Evaluation of reference genes for real-time quantitative PCR studies in *Candida glabrata* following azole treatment. *BMC Mol. Biol.* **2012**, *13*, 22. [CrossRef]
31. Hou, X.; Healey, K.R.; Shor, E.; Kordalewska, M.; Jimenez-Ortigosa, C.; Paderu, P.; Xiao, M.; Wang, H.; Zhao, Y.; Lin, L.Y.; et al. Novel *FKS1* and *FKS2* modifications in a high-level echinocandin resistant clinical isolate of *Candida glabrata*. *Emerg. Microbes Infect.* **2019**, *8*, 1619–1625. [CrossRef]
32. Mastronarde, D.N. Automated electron microscope tomography using robust prediction of specimen movements. *J. Struct. Biol.* **2005**, *152*, 36–51. [CrossRef] [PubMed]
33. Zheng, S.Q.; Palovcak, E.; Armache, J.P.; Verba, K.A.; Cheng, Y.; Agard, D.A. MotionCor2: Anisotropic correction of beam-induced motion for improved cryo-electron microscopy. *Nat. Methods* **2017**, *14*, 331–332. [CrossRef]
34. Chen, M.; Bell, J.M.; Shi, X.; Sun, S.Y.; Wang, Z.; Ludtke, S.J. A complete data processing workflow for cryo-ET and subtomogram averaging. *Nat. Methods* **2019**, *16*, 1161–1168. [CrossRef]
35. Rosenthal, P.B.; Henderson, R. Optimal Determination of Particle Orientation, Absolute Hand, and Contrast Loss in Single-particle Electron Cryomicroscopy. *J. Mol. Biol.* **2003**, *333*, 721–745. [CrossRef] [PubMed]
36. Pettersen, E.F.; Goddard, T.D.; Huang, C.C.; Couch, G.S.; Greenblatt, D.M.; Meng, E.C.; Ferrin, T.E. UCSF Chimera—A visualization system for exploratory research and analysis. *J. Comput. Chem.* **2004**, *25*, 1605–1612. [CrossRef]
37. Rico, H.; Carrillo, C.; Aguado, C.; Mormeneo, S.; Sentandreu, R. Initial steps of wall protoplast regeneration in *Candida albicans*. *Res. Microbiol.* **1997**, *148*, 593–603. [CrossRef]
38. Okada, H.; Abe, M.; Asakawa-Minemura, M.; Hirata, A.; Qadota, H.; Morishita, K.; Ohnuki, S.; Satoru Nogami, S.; Ohya, Y. Multiple Functional Domains of the Yeast l,3-β-Glucan Synthase Subunit Fks1p Revealed by Quantitative Phenotypic Analysis of Temperature-Sensitive Mutants. *Genetics* **2010**, *184*, 1013–1024. [CrossRef] [PubMed]
39. Okada, H.; Ohnuki, S.; Roncero, C.; Konopka, J.B.; Ohya, Y. Distinct roles of cell wall biogenesis in yeast morphogenesis as revealed by multivariate analysis of high-dimensional morphometric data. *Mol. Biol. Cell.* **2014**, *25*, 222–233. [CrossRef] [PubMed]
40. Purushotham, P.; Ruoya, H.; Zimmer, J. Architecture of a catalytically active homotrimeric plant cellulose synthase complex. *Science* **2020**, *369*, 1089–1094. [CrossRef] [PubMed]